Shielding Gas and Inclusion Content Effects on Impact Toughness and Tensile Properties of 410NiMo Steel Welds

The effect of shielding gas on the mechanical and microstructural characteristics of ER410NiMo martensitic stainless steel weldments was investigated

BY B. TENNI, S. GODIN, D. THIBAULT, AND M. BROCHU

ABSTRACT

The effect of shielding gas on the mechanical and microstructural characteristics of ER410NiMo martensitic stainless steel weldments was investigated. Three weldments with various inclusion contents were manufactured using different shielding gas compositions and welding processes: gas metal arc welding (GMAW) with 100% argon (Ar), GMAW 85% Ar/15% carbon dioxide (CO_2), and flux cored arc welding (FCAW) 75% Ar/25% CO_2.

The inclusions in each weldment were characterized by means of scanning electron microscope observations and energy-dispersive spectroscopy analysis. The weldments underwent postweld heat treatment, after which the chemical composition and reformed austenite proportion were measured to account for microstructural effects. Hardness measurements, tensile tests, and impact toughness tests using the Charpy method were performed. The results showed that the Charpy V-notch (CVN) absorbed energy decreases with increasing inclusion content. The highest CVN absorbed energy, 195 J, was obtained for the GMAW 100% Ar weld, which had the lowest inclusion content. GMAW 85% Ar/15% CO_2, with four times more inclusions than the former, had a CVN absorbed energy of 63 J. The current manufacturing process, FCAW 75% Ar/25% CO_2, was found to have an inclusion content three times higher than the GMAW 100% Ar weld but a CVN absorbed energy of 66 J, which is close to the GMAW 85% Ar/15% CO_2 weld. The results showed that using GMAW 100% Ar as a replacement to FCAW 75% Ar/25 % CO_2 would lead to a three-fold improvement in terms of absorbed impact energy.

The effect of inclusions on tensile properties, which was not clearly identified as several factors, in addition to inclusion content, affects the weld strength and elongation. Overall, the yield and ultimate tensile strengths differed slightly: 724 and 918 MPa for GMAW 100% Ar, 746 and 927 MPa for GMAW 85% Ar/15% CO_2, and 711 and 864 MPa for FCAW 75% Ar/25% CO_2, respectively.

KEYWORDS

• Martensitic Stainless Steel • Inclusions • Welding
• Impact Toughness

Introduction

ER410NiMo is a low-carbon 13% Cr–4% Ni soft martensitic stainless steel. This filler metal is considered to be the best match to CA6NM base metal, which is the cast version of this steel.

For hydraulic turbine runners, which are the application of interest in this paper, several properties are important. These include good fatigue properties, corrosion resistance, cavitation erosion resistance, and weldability, as well as ease of casting. These requirements are satisfactorily met by soft martensitic stainless steels, which is the reason for their growing popularity in the hydropower industry.

Weldability and fatigue properties of weldments are especially important for hydraulic turbine runner manufacturers, because runners are assembled by welding, and for power plant owners because they often have to carry out on-site repairs of cavitation and fatigue damages through welding.

Welded regions, however, have particular features such as undesired residual stresses, welding discontinuities, and inclusions. Moreover, as demonstrated by Amrei et al. (Ref. 1), martensitic stainless steel weldments are characterized by a complex and heterogeneous microstructure due to the existence of coarse and fine-grain regions in the weld.

Currently, arc welding processes are used to assemble hydraulic turbine runners. The assembly process consists of welding the blades to the crown and belt. Current practices use the flux cored arc welding (FCAW) process with a shielding gas of 75% argon (Ar)/25% carbon dioxide (CO_2). To test the influence of oxides on mechanical properties, gas metal arc welding (GMAW) was used with two different shielding gas compositions and compared to current FCAW procedures. Procedures using shielding gases with more CO_2 trap more oxygen in the molten pool. This is due to the electric arc and the high temperatures involved during the welding operation, which lead to ionization of CO_2 decomposes into *C* and *O*, resulting in more oxygen in the weld pool. This oxygen is then free to form oxides through reactions with other alloying elements.

Teske and Martins (Ref. 2) conducted a study on the influence of shielding gas composition in GMAW using different mixtures with either CO_2 or O_2. When present, CO_2 and

https://doi.org/10.29391/2021.100.005

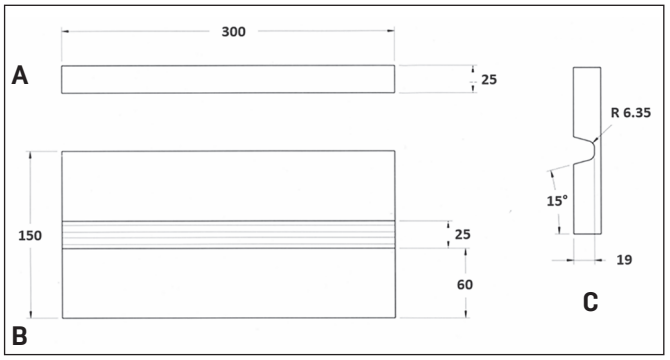

Fig. 1 — Dimensions, in millimeters, of the bare plates: A — Side view; B — view from the top of the weld; C — profile showing the U-notch.

Table 1 — Welding Conditions Used to Prepare the Weldments for Impact Toughness Testing

	GMAW 100% Ar	GMAW 85% Ar/ 15% CO_2	FCAW 75% Ar/ 25% CO_2
Voltage (V)	25	28.8	27.5
Current (A)	210	207.5	228
Torch speed (mm/s)	3.8	3.8	4.2
Heat input (J/mm)	1381	1572	1505
Number of weld beads	11	10	12

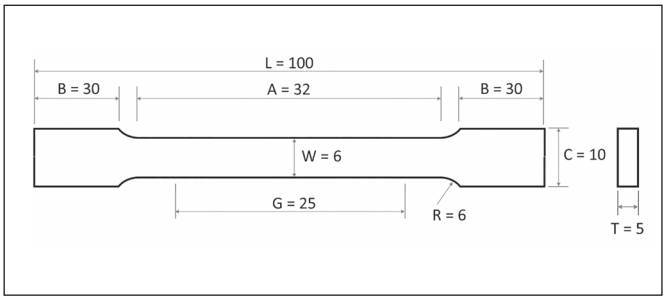

Fig. 2 — Tensile test specimen geometry (mm). Prior to testing, two points were punched 1 in. apart to establish the original length and calculate the elongation at fracture.

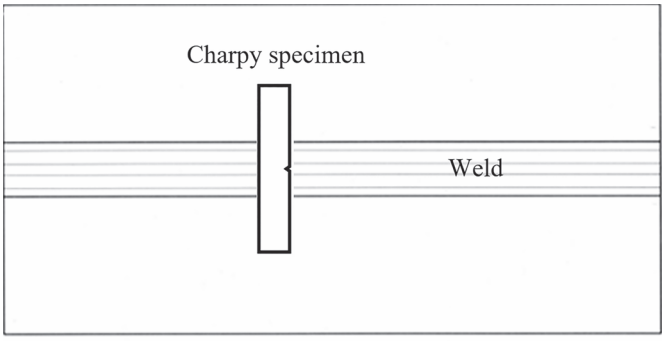

Fig. 3 — Schematic drawing showing the Charpy specimen orientation with respect to the weld.

O_2 cause the formation of oxide inclusions due to their oxidation potential; note that the oxidation potential is twice as high for O_2 than it is for CO_2. The welds with the highest occurrence of oxides showed the lowest impact toughness properties. Foroozmehr et al. (Ref. 3) examined the effect of inclusions on the impact toughness properties of two 13% Cr–4% Ni martensitic stainless steels, a cast version (CA6NM) and a wrought one (UNS S41500). The results showed that the higher content and the larger mean size of inclusions in CA6NM explained the lower impact toughness properties compared to UNS S41500. This was justified by microvoid formation from the inclusions.

Other metallurgical factors should also be accounted for when studying such steels. Though the microstructure is mostly martensitic, small amounts of delta ferrite and austenite are usually present and can affect mechanical properties. Delta ferrite, for example, is oftentimes considered detrimental to mechanical properties, especially in terms of fracture toughness and impact absorbed energy. Iwabuchi and Kobayashi (Ref. 4) attributed the deleterious effect of delta ferrite to the precipitation of carbides along delta-ferrite grain boundaries during heat treatment. To minimize the negative effect of delta ferrite, nickel, which is an austenite-stabilizing element, is added to chromium martensitic stainless steels to keep a martensitic microstructure, thus preventing carbides from precipitating. However, due to carbide precipitation along delta-ferrite grain boundaries, it is difficult to isolate the effect of delta ferrite from that of carbides as Wang et al. (Ref. 5) brought to attention.

By successfully isolating both effects, the authors concluded that delta-ferrite only influences the transition temperature region in terms of impact absorbed energy, and it does not have a significant effect on the upper- and lower-shelf energies. Aside from delta ferrite, another phase that can be present is retained austenite; usually only a very small fraction remains present after quenching. However, during tempering heat treatment, a greater amount of austenite can be reformed. Bilmes et al. (Ref. 6) studied tempering of martensitic stainless steel as well as the austenite resulting from such a treatment. It was found that the reformed amount can reach up to 30% in the form of finely precipitated at the prior austenite grain boundaries. This phase is believed to improve toughness and ductility of the studied steels. When tempering slightly above Ac_1, the reformed austenite is thermally stable and leads to optimal mechanical properties. Tempering at higher temperatures leads to the formation of unstable austenite, which transforms to fresh martensite upon cooling. However, under applied load, even thermally stable austenite can transform back to martensite, which makes austenite mechanically unstable. This mechanism is commonly known as the transformation-induced-plasticity (TRIP) effect and is responsible for the interesting mechanical properties resulting from reformed austenite. Thibault et al. (Ref. 7) studied this aspect, concluding that when the TRIP mechanism occurs, more energy is required for the fracture process due to the volumetric expansion accompanying the austenite to martensite transformation, which induces compressive stresses at the crack tip.

In addition to creating reformed austenite, tempering post-weld heat treatment relieves residual stresses in the weld and the heat-affected zone (HAZ) as well as softens the hard and brittle as-welded martensite as demonstrated in the work of Trudel et al. (Ref. 8) performed on welded CA6NM.

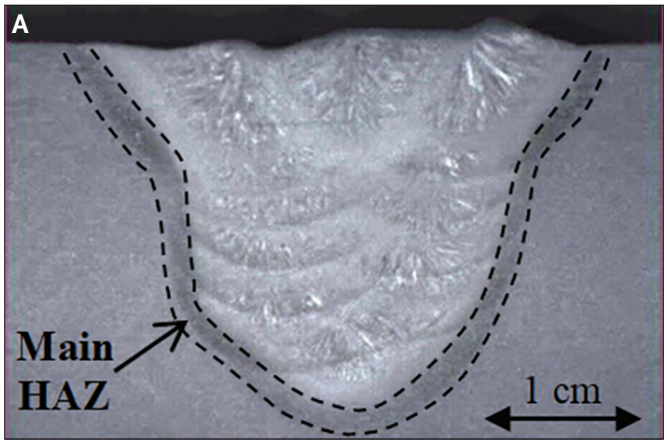

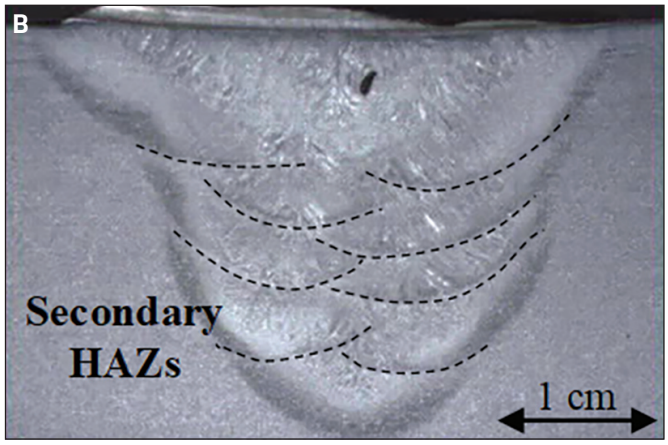

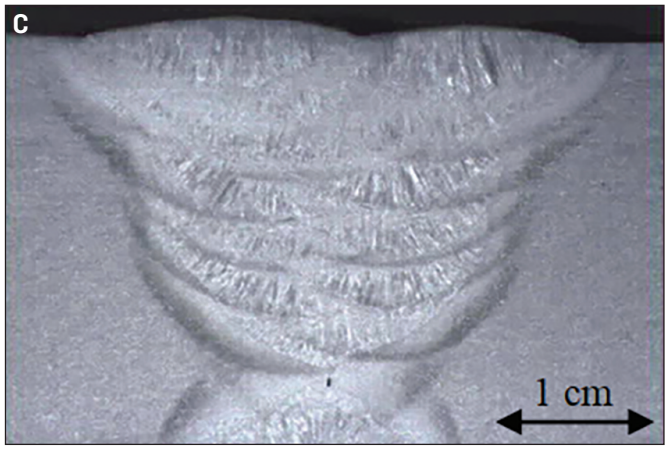

Fig. 4 — Macrographs of the postweld heat treated welds: A — GMAW 100% Ar; B — GMAW 85% Ar/15% CO_2; C — FCAW 75% Ar/25% CO_2.

Table 2 — Welding Conditions Used to Prepare the Weldments Destined for Tensile Testing

	GMAW 100% Ar	GMAW 85% Ar/15% CO_2	FCAW 75% Ar/ 25% CO_2
Voltage (V)	24.3	26.5	27.5
Current (A)	212	222	222
Torch speed (mm/s)	3.9	3.9	4.2
Heat input (J/mm)	1320	1508	1453

The aim of the research presented in this paper is to study the effect of shielding gas composition on the impact toughness and tensile properties of martensitic stainless steel weldments. The weldments made using different welding processes and shielding gas compositions produced varying inclusion contents.

Experimental Methodology

Materials

The welding procedure used FCAW with a shielding gas composition of 75% Ar/25% CO_2.

As discussed in the introduction, this relatively high content of CO_2 is believed to cause the formation of oxides, shown to negatively affect mechanical properties. Since GMAW requires less active gas in the shielding mixture, it was used to produce welds under different shielding gas compositions, which in turn resulted in different oxide contents. Hence, three welds were produced under the following atmospheres:

- FCAW 75% Ar/25% CO_2, the current process in use;
- GMAW 100% Ar, the process thought to generate the least oxide content and;
- GMAW 85% Ar/15% CO_2, an intermediate condition for research purposes.

Figure 1 gives the dimensions of the CA6NM plates that were used to produce the welds destined to machine the Charpy specimens. The U-notch preparation presented in Fig. 1C has been filled by multipass robotized welding with an AWS ER410NiMo filler metal wire of 1.6 mm in diameter.

Table 1 provides the welding conditions used in each procedure. An effort was made to keep the heat input energy constant in the three procedures because it directly affects the temperatures and, as a result, the weld microstructure. The objective was to vary the oxide content while keeping all other influencing factors constant.

Additional weldments were prepared by depositing weld metal on the entire surfaces of the plates. This is done to ensure the tensile test specimens are fully extracted from the weld metal. The same filler metal was used but the base metal was UNS-S41500, which is the wrought version of CA6NM used previously. Because UNS-S41500 and CA6NM have comparable chemical compositions, it was expected that the tensile properties of the second batch of welded plates were also characteristic of the first one. Table 2 gives the welding conditions used for this second batch.

Postweld Heat Treatment

After welding, the plates underwent a tempering postweld heat treatment at 600°C for a duration of 20 h. The furnace atmosphere was not controlled.

Austenite Measurements

After postweld heat treatment, the proportions of austenite were measured by x-ray diffraction from a Rietveld analysis (Ref. 9). The x-ray diffraction patterns were obtained with a Bruker D8 Advance diffractometer equipped

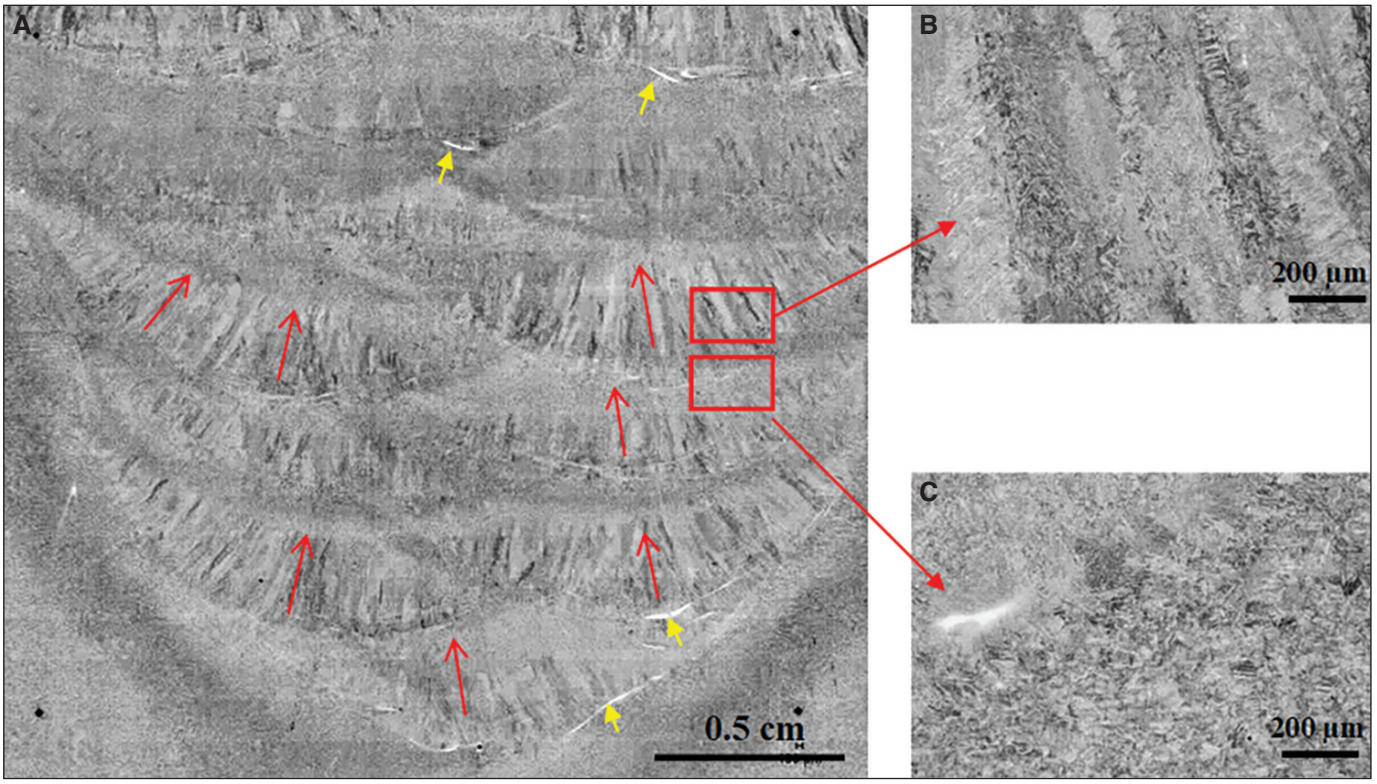

Fig. 5 — Weld microstructure observed in FCAW 75% Ar/25% CO_2 postweld heat treated: A — Macrograph of the weld; B — magnified view displaying a column-shaped martensite; C — magnified view displaying a HAZ with finer grains. The red arrows show the orientation of martensite columns, corresponding to the heat flow directed toward the top of the weld.

with a copper x-ray tube and a nickel filter. The measurements were done on thin slices cut transverse to the welds. Three samples per weld were prepared.

Chemical Composition Measurements

The chemical composition of both types of filler metals (solid wire and flux-cored wire), as well as the base metal and each of the fusion zones of the welds described above, were measured by inductively coupled plasma-emission atomic spectrometer in accordance with ASTM E1479 (Ref. 10) except for carbon, sulfur, oxygen, and nitrogen contents measured by combustion and inert gas fuel (ASTM E1019).

Hardness Measurements

To evaluate the hardness of the welds, and ensure the three welds were equivalent in terms of hardness, ten Vickers hardness measurements were made in each weld using a ZwickRoell ZHU 250 hardness tester in the transverse direction as well as in the as-welded and tempered conditions at 10 kgf in accordance with ASTM E92 (Ref. 12).

Quantification of Oxides

Metallographic cross sections cut transverse to the weld were prepared. Using a scanning electron microscope (SEM) Hitachi S-4700 equipped with an energy dispersive spectrometer (EDS), the oxides were observed, counted, and analyzed through EDS analysis. In total, 16 images at a 5000x magnification were used, yielding a total examined surface of seven 200 μm^2 for GMAW 85% Ar/15% CO_2 and FCAW 75% Ar/25% CO_2 welds. As for GMAW 100% Ar, extra images were taken to ensure at least 100 oxides were counted, yielding a total surface of 15 338 μm^2. For each observed oxide, the horizontal and vertical ferrets were measured, and the mean of both measurements was considered to produce size distribution spectra.

Tensile Testing

Three tensile tests per condition were realized in the weld metal in the transverse direction with respect to the deposited weld beads. A MTS Systems tensile tester model Exceed 40 using a 50-kN load cell was used. A MTS extensometer model 632.24-50 with a gauge length of 25 mm was used to monitor the elongation. The displacement rate was 2 mm/min, leading to a strain rate of about 0.06/min.

Figure 2 shows the geometry and dimensions of the test specimens, which correspond to an ASTM E8 (Ref. 13) subsize specimen.

Impact Toughness Properties

To perform impact toughness tests, five Charpy V-notch (CVN) bars of standard dimensions $10 \times 10 \times 55$ mm were machined from each weld. Impact tests were performed at 0°C, with a ZwickRoell RKP450 pendulum impact tester in accordance with ASTM E23 (Ref. 14). The specimens were

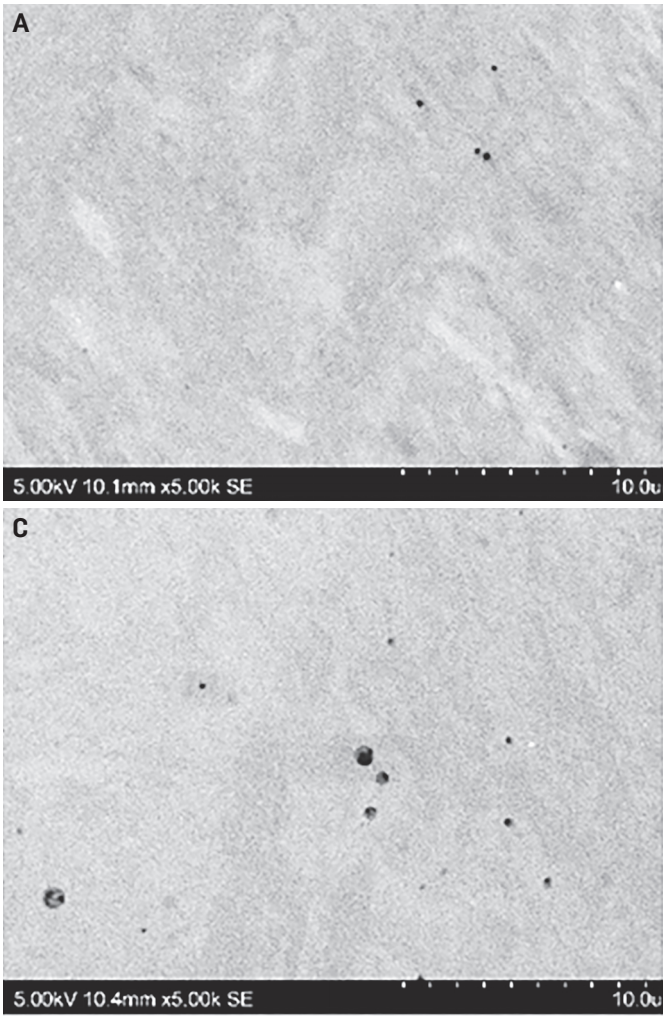

Fig. 6 — SEM images of as-polished cross sections transverse to the welds displaying oxides: A — GMAW 100% Ar; B — GMAW 85% Ar/15% CO_2; C — FCAW 75% Ar/25% CO_2.

machined in the transverse direction, in the center of the weld, as shown in Fig. 3.

Results and Discussion

Chemical Composition

Table 3 gives the measured chemical compositions of each weld and the specified chemical compositions for comparison. The measured chemical compositions are all compliant with the specifications, except for the manganese content in the 410NiMo solid wire and both GMAW welds. The higher-than-specified Mn content in the GMAW weldments is therefore most probably due to the high Mn content found in the corresponding filler metal, which might affect the austenite content because Mn is an austenite-promoting element. Also, GMAW 85% Ar/25% CO_2 has a slightly lower-than-specified Ni content, which might also affect the austenite content because nickel is an austenite-promoting element. Note that the carbon and oxygen contents are significantly higher in GMAW 85% Ar/15% CO_2 compared to the other welds.

Reformed Austenite Measurements

Table 4 provides the mean percentage of austenite and the standard deviation obtained from the measurements in each weld. These measurements include both residual and reformed austenite, but since residual austenite proportion is not expected to exceed 1% as measured by Godin (Ref. 17), the obtained proportions give a good indication on the amount of reformed austenite.

To compare the weldments in terms of the extent of their austenitic domain, hence their ability to create reformed austenite when tempered at 600°C, an estimation of their Ac_1 temperature was obtained using an empirical equation proposed by Gooch et al. (Ref. 18). The equation shows the effect of austenite-promoting elements (C, N, Ni, Mn) and ferrite-promoting elements (Si, Mo, Cr) on the Ac_1 temperature. Theoretically, if Ac_1 of a material reported in Table 4 is above 600°C, no austenite should reform during tempering. Below 600°C, the lower the Ac_1 of a given material is, the greater the proportion of austenite is expected to reform during tempering.

$$Ac_1(°C) = 850 - 1500(C + N) - 50\,Ni - 25\,Mn + 25\,Si + 25\,Mo + 20(Cr - 10) \quad (1)$$

The theoretical Ac_1 temperature was calculated using Equation 1 and the measured chemical composition given in Table 1. The results of these calculations are provided in Table 4.

Assuming the austenite reformed while tempering was stable at room temperature, its proportion should be maximum in the GMAW 85% Ar/15% CO_2 weld and inexistent in the FCAW 75% Ar/25% CO_2 weld. Nevertheless, the x-ray diffraction analysis showed more than 20% of austenite in all welds, with the highest amount in the FCAW 75% Ar/25% CO_2. This indicated Equation 1 cannot be used to estimate the austenite content of the studied welds.

The raw results that led to empirical Equation 1 have not been detailed in the work of Gooch et al. It was most probably based on homogeneous material chemistry and specific heating rates. Because of the potential differences between the experimental conditions, Equation 1 can hardly predict

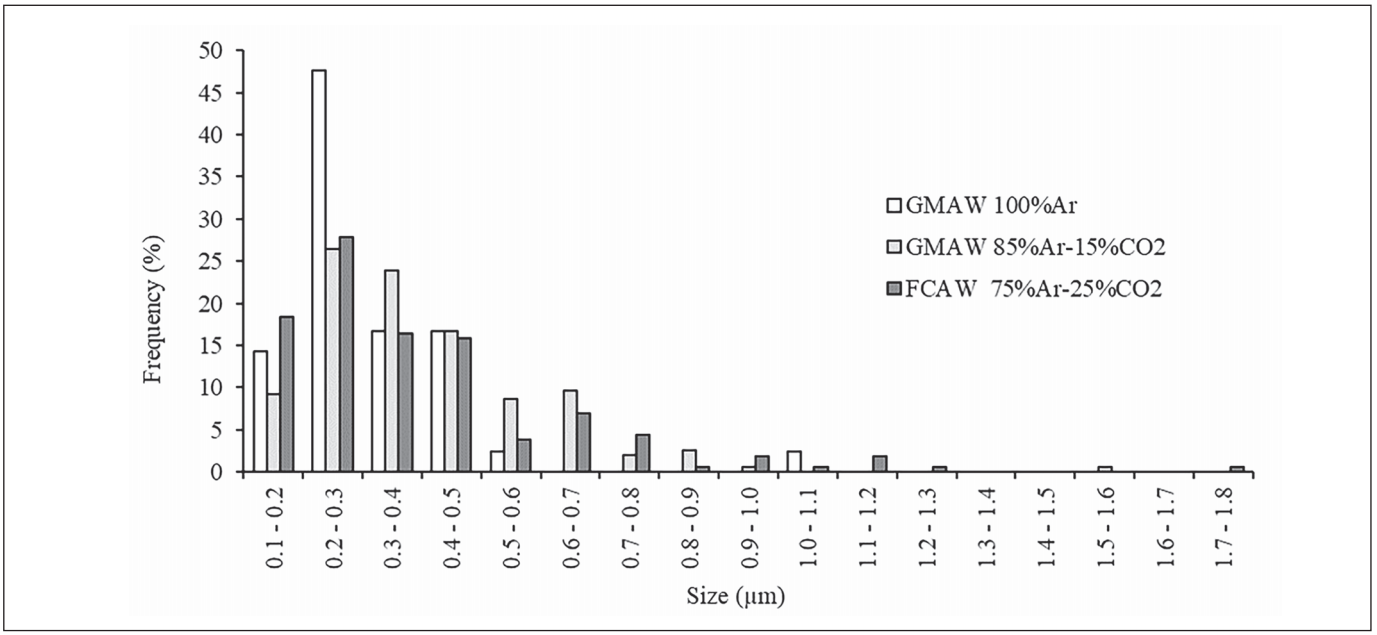

Fig. 7 — Size distribution of oxides.

the austenite content in the studied cases. The amount of austenite measured in the FCAW 75% Ar/25% CO_2 weld is close to the maximum amount reported by Bilmes et al. (Ref. 6), who specifically studied the formation and stability of reformed austenite 13Cr–NiMo martensitic steel weld metals.

Microstructure of the Welds

Figures 4 and 5A show macrographic views of the prepared metallographic cross sections of the the postweld heat treated welds, etched with Vilella's reagent. The main HAZ, as well as the secondary ones in between weld beads, is visible on the

Table 3 — Chemical Compositions of ER410NiMo and CA6NM as per Material Specifications and Measured Chemical Compositions of the Welds, Base Metal, and Filler Metals (wt-%)

		% C	% S	% O	% N	% P	% Si	% Mn	% Cr	% Ni	% Mo
Specified	Base metal CA6NM (Ref. 15)	0.06 max.	0.03 max.	N.S.[1]	N.S.	0.04 max.	1.0 max.	1.0 max.	11.5–14	3.5–4.5	0.4–1.0
	ER410NiMo (Ref. 16)	0.06 max.	0.03 max.	N.S.	N.S.	0.03 max.	0.5 max.	0.6 max.	11.0–12.5	4.0–5.0	0.4–0.7
Measured	Base metal CA6NM	0.033	0.0005	0.002	0.031	0.021	0.46	0.65	12.5	4.10	0.634
	410NiMo (solid wire for GMAW)	0.018	0.001	N.M.[2]	0.028	0.019	0.38	0.70	12.4	4.14	0.500
	410NiMo (flux-cored wire for FCAW)	0.021	0.011	N.M.	N.M.	0.008	0.37	0.36	12.5	4.39	0.560
	GMAW 100% Ar	0.024	0.002	0.013	0.036	0.027	0.41	0.77	12.3	4.04	0.546
	GMAW 85% Ar/ 15% CO_2	0.043	0.001	0.068	0.031	0.018	0.33	0.64	12.2	3.89	0.544
	FCAW 75% Ar/ 25% CO_2	0.026	0.007	0.070	0.01	0.018	0.38	0.44	12.0	4.30	0.605

[1] Not specified
[2] Not measured

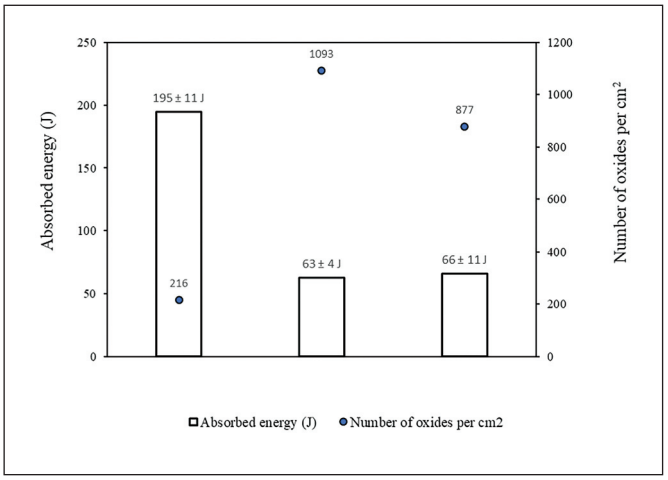

Fig. 8 — Charpy absorbed energy results and the oxide density in each weld.

macrographs due to its darker aspect. As observed, an effort was made to have similar weld pool and overall weld dimensions to create a comparable weld microstructure.

Figure 5B and C provides a magnified view of the FCAW 75% Ar/25% CO_2 postweld heat treated weld macrograph. Regions of columnar martensite, consisting of column-shaped packets, are shown in Fig. 5B separated by fine-grain regions as in Fig. 5C. A similar grain structure was observed by Amrei et al. (Ref. 19) in ER410NiMo filler metal deposited by FCAW using 75% Ar/25% CO_2. Note that martensite columns appear to be pointing to the top of the weld as depicted by the red arrows, which corresponds to the heat flow direction. Reformed austenite is not visible by optical microscopy because it is finely (60 to 200 nm wide) distributed between the martensite lath, as shown in other work performed on comparable material (Ref. 22).

Although it was not confirmed, the fine white stringers, observed in Fig. 5A and C indicated by the smaller yellow arrows, are most likely delta-ferrite stringers because they look similar to what was reported by Thibault et al. (Ref. 20) and Foroozmehr et al. (Ref. 3).

Table 4 — Mean Percentage of Austenite (% γ) with the Standard Deviation of the Measurements and Theoretical AC_1 Temperature

	% γ	AC_1 (°C)
GMAW 100% Ar	21 ± 1	609
GMAW 85% Ar/15% CO_2	25 ± 2	594
FCAW 75% Ar/25% CO_2	27 ± 1	634

Table 5 — Hardness and Standard Deviation of the Weldments Before and After Tempering Postweld Heat Treatment

	Mean HV10	
	As welded	Tempered
GMAW 100% Ar	356 ± 20	292 ± 5
GMAW 85% Ar/15% CO_2	368 ± 23	283 ± 8
FCAW 75% Ar/25% CO_2	327 ± 18	281 ± 8

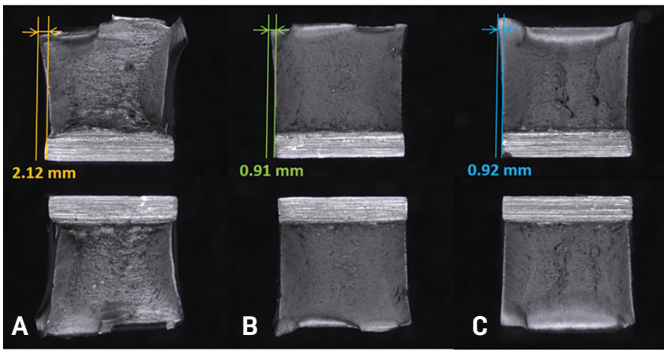

Fig. 9 — Fracture surfaces of Charpy V-notch specimens with the corresponding lateral expansions: A — GMAW 100% Ar; B — GMAW 85% Ar/15% CO_2; C — FCAW 75% Ar/25% CO_2.

Hardness

Table 5 gives the Vickers hardness measurements for each weld in both the as-welded and tempered conditions.

The obtained results show the softening effect of the tempering heat treatment. In each of the three welding conditions, the mean hardness decreased by 18%, 23%, and 14% after tempering. The standard deviation was reduced as well for all welds, suggesting a more uniform microstructure. Considering the standard deviations, the hardness intervals of the welds overlap, which means the welds can be considered comparable in terms of hardness.

Oxides Characterization

Figure 6 shows SEM images of as-polished cross sections cut transverse to the welds displaying oxides, which identification of was confirmed through detection of oxygen in EDS analyses.

Table 6 gives the quantification results, namely the number of oxides per 100 mm^2, the mean size of oxides, as well as the median size for each weld.

To verify if there are any significant differences between the welds in terms of inclusion size, an analysis of variance (ANOVA) test was used. This test is used to compare multiple statistical groups and determine whether they significantly differ. Setting the P value of the ANOVA test to 5%, we can't reject the hypothesis that all means are equal. This shows that it is not possible to consider with confidence the mean values of the oxides as different.

As expected, the GMAW 100% Ar had the lowest oxide content. However, the FCAW 75% Ar/25% CO_2 didn't have the highest oxide content, despite having the highest CO_2 concentrated shielding gas. This can be explained by the presence of

Table 6 — Oxides Median Size, Mean Size, and Density

	Median Size (μm)	Mean Size (μm)	Number of Oxides per cm^2
GMAW 100% Ar	0.39	0.49	216
GMAW 85% Ar/15% CO_2	0.36	0.40	1093
FCAW 75% Ar/25% CO_2	0.32	0.40	877

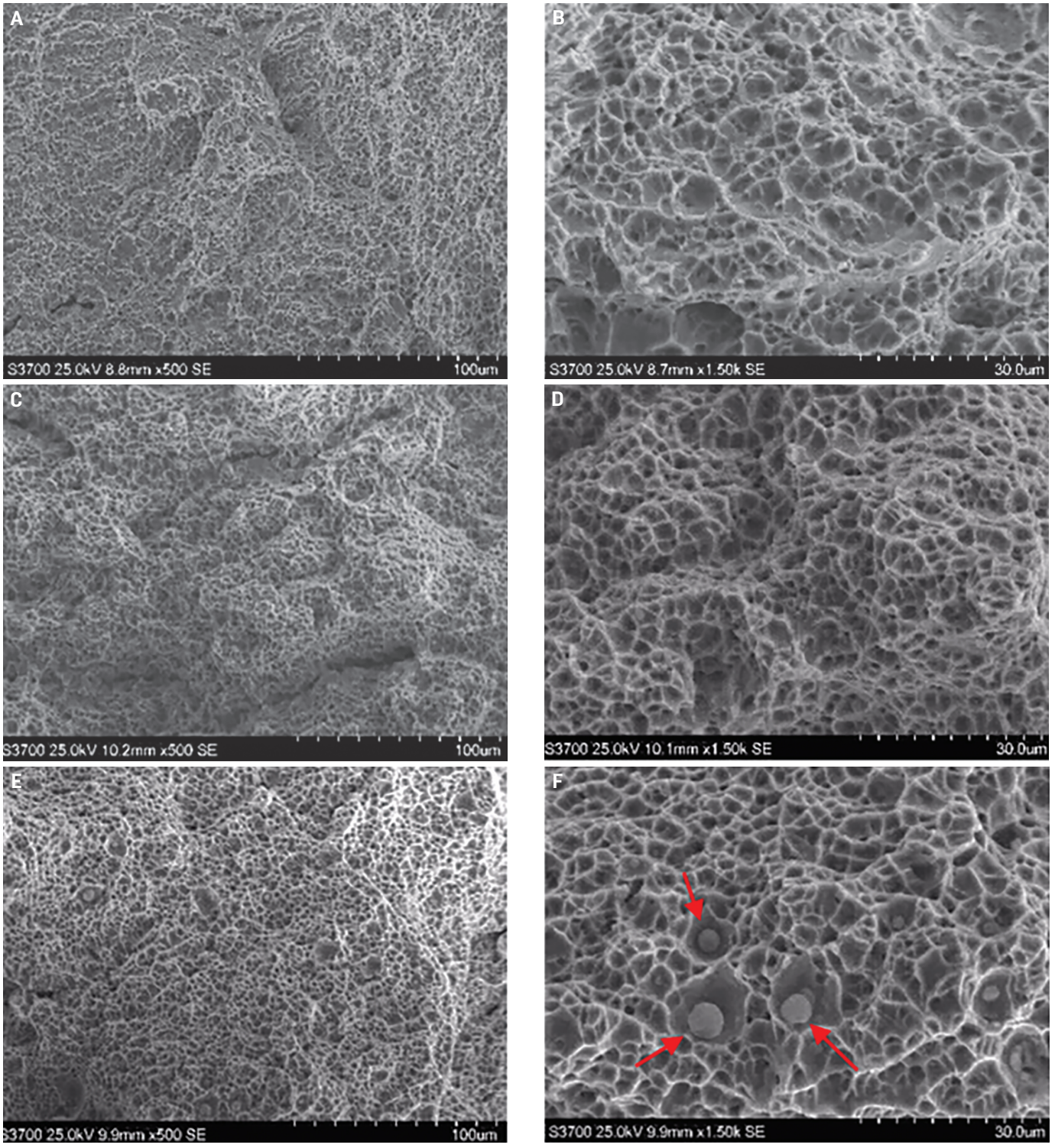

Fig. 10 — Dimpled fracture on Charpy fracture surfaces: 500x magnification: A, B — GMAW 100% Ar; C, D — GMAW 85% Ar/15% CO_2; E, F — FCAW 75% Ar/25% CO_2 at magnifications of 500x and 1500x, respectively.

Table 7 — Elements Present in the Oxides

	O	Si	Cr	Mn	Al	Mg	Ca	Ti	Zr
GMAW	x	x	x	x	x	x	x		
FCAW	x	x	x	x				x	x

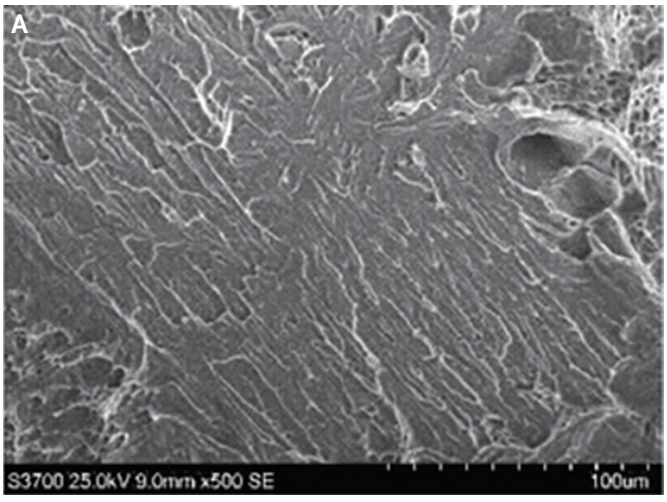

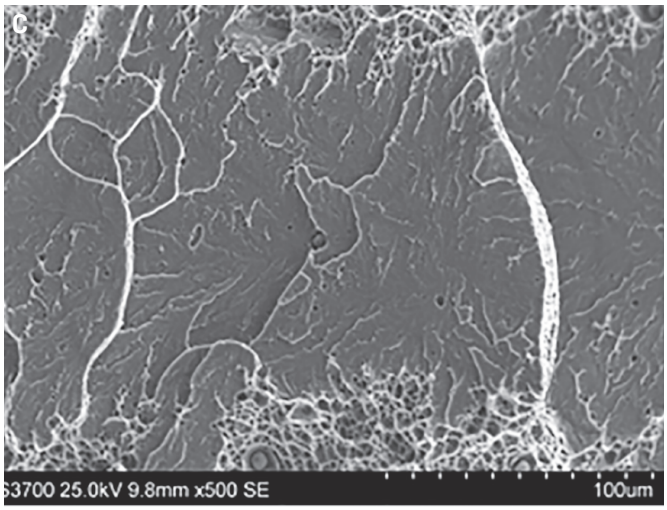

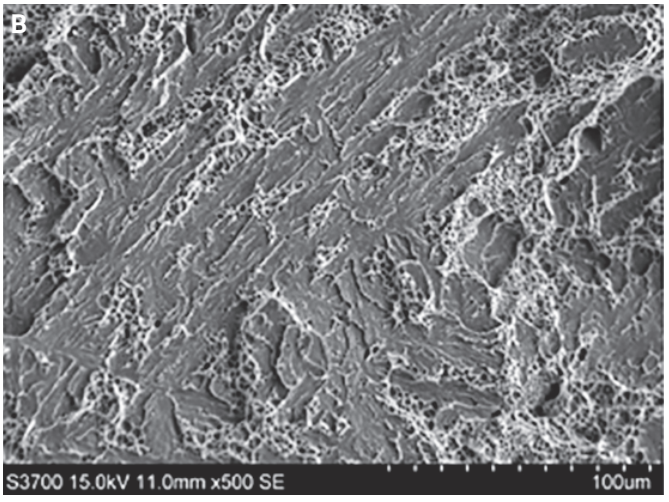

Fig. 11 — Examples of cleavage observed on fracture surfaces: A — GMAW 100% Ar; B — GMAW 85% Ar/15% CO_2; C — FCAW 75% Ar/25% CO_2.

the flux, which protects the weld pool from oxidation.

Figure 7 displays the size distribution of the measured oxides for each welding process. For all three welds, the class with the highest number of oxides is 0.2–0.3 µm.

The chemical composition of the oxides was determined using the EDS spectrometer coupled with the SEM. Though this method is standardless and semiquantitative, it gives a good idea about the chemical composition of the oxides. The analysis showed both GMAW welds to have oxides with similar compositions, but the FCAW weld had slightly different oxides. Table 7 gives the elements present in the weld oxides from both welding processes.

This difference between GMAW and FCAW might be caused by the elements present in the flux. Foroozmehr et al. (Ref. 3) reported that Si/Mn inclusions have a lower resistance against rupture and microvoid formation than Al inclusions (both types seem to be present in the GMAW welds) whereas Al inclusions weren't detected in FCAW.

Tensile Properties

Table 8 gives the means and standard deviations obtained from the tensile properties retrieved from the stress-strain curves following ASTM E8 (Ref. 13) recommendations.

Three material characteristics that could influence the weld's mechanical behavior are presented in Table 8: the inclusion content, the percentage of reformed austenite, and the carbon content. Indeed, the inclusion content was shown to be detrimental to the material ductility as reported by Foroozmehr et al. (Ref. 3), who compared the mechanical behavior and microstructure of CA6NM and UNS41500. Reformed austenite, on the other hand, is believed to increase the steel yield strength and ductility due to the TRIP mechanism. As for the carbon content, Krauss (Ref. 21) showed that the yield stress of low-carbon martensite has a square-root dependency with the solute carbon content. Despite having the largest inclusion content, GMAW 85% Ar /15% CO_2 shows the highest yield and tensile strengths without a significant drop of ductility when compared with the GMAW 100% Ar weld characterized by the lowest inclusion content. The higher carbon content within the GMAW 85% Ar/15% CO_2 weld, 0.043% vs. 0.024% and 0.026% for GMAW 100% Ar and FCAW 75% Ar/25% CO_2, could explain its higher strength. Moreover, the percentage of reformed austenite measured in this weldment was 25%, compared to 21% for GMAW 100% Ar, which could have compensated for a potential ductility loss caused by the presence of inclusions.

Table 8 — Tensile Properties of the Welds

Weld	$\sigma_{y\ 0.2\%}$	σ_{UTS}	A (%)
GMAW 100% Ar	724 ± 7	918 ± 1	21 ± 1
GMAW 85% Ar/15% CO_2	746 ± 11	927 ± 4	19 ± 1
FCAW 75% Ar/25% CO_2	711 ± 32	864 ± 1	19 ± 5

The FCAW 75% Ar/25% CO_2 weld also had a quite large inclusion content, but it is also characterized by the highest amount of austenite. In this case, as for GMAW 85% Ar/15% CO_2, it could explain that no significant decrease in ductility was observed.

Impact Toughness Properties

Figure 8 gives the CVN absorbed energy and the oxide density, while Fig. 9, the measured lateral expansions, illus-

trates the fracture surfaces. Given the results of Fig. 8, it seems that the inclusion content is the dominant influencing factor on CVN absorbed energy because the absorbed energy decreased with increasing inclusion content. GMAW 100% Ar with the lowest inclusion content had the highest absorbed energy, three times that of the other two conditions.

Measurements of the lateral expansion were realized on the fractured Charpy specimens and are illustrated in Fig. 9 with the fracture surfaces. As can be seen on the image, there is a good agreement between the absorbed energy and the measured lateral expansion: the higher the absorbed energy, the greater the deformation, hence, the lateral expansion.

The fracture surfaces were examined using a SEM to determine fracture mechanisms. SEM fractography revealed the fracture to be mostly ductile as evidenced by the dimpled rupture. Examples are displayed in Fig. 10.

All three welds exhibited some cleavage areas toward the center of the fracture surfaces. Examples are shown in Fig. 11. Although cleavage is usually suggestive of brittleness, it is not always the case. The center of the specimens represents the location of the highest hydrostatic stresses, which promotes cleavage fracture, even if the temperature is above the ductile-to-brittle transition temperature.

Based on the previous observations, the main fracture mechanism is microvoid formation and coalescence, as for most ductile materials. All oxides observed on the fracture surfaces are found sitting inside the dimples (as shown by red arrows in Fig. 10), suggesting the dimples nucleated at oxides.

Therefore, the effect of oxides on absorbed energy can be discussed as follows: In the case of a large inclusion content, void nucleation from oxide inclusions is the dominant mechanism, and the growth stage is instantaneous. However, when fewer oxides are present, fewer nucleation sites are available, making the growth stage dominant. This leads to higher deformation, and consequently, a more energy-consuming fracture.

The findings are consistent with the study of Foroozmehr et al. (Ref. 3), where the higher mechanical properties of the wrought steel were attributed to the lower inclusion content, lower mean size of inclusions, and type of inclusions; those in the wrought steel were found more resistant against rupture than the ones in the cast steel. As the size of the inclusions was found equivalent in the three studied welds, it was possible to isolate the effect of the inclusion density.

Conclusion

In light of the work described in this article, the following conclusions can be drawn:

1) A shielding gas with a higher concentration of CO_2 increases oxide content in the weld. If the current welding procedure using FCAW is to be replaced by GMAW under pure argon, oxide content could be decreased by a factor of three.

2) As far as impact toughness properties are concerned, replacing the FCAW 75% Ar/25% CO_2 process, which is the current manufacturing process, with the GMAW 100% Ar process would lead to a three-fold improvement.

3) CVN absorbed energy decreases as oxide content increases. A high inclusion content increases nucleation sites for microvoids, and coalescence then leads to rapid damage and rupture. On the other hand, a low inclusion content means less nucleation sites, which leads to more plastic deformation during the growth stage, resulting in higher absorbed energy.

In view of these three conclusions, for application where impact resistance is critical, it is recommended to weld 410NiMo with GMAW using a shielding gas composed of 100% argon because it limits the formation of inclusions that are detrimental to impact energy absorption. Though small variations were observed in tensile properties, it seemed that several factors were competing, namely the carbon, austenite, and inclusion content. Verification of the effect of each factor is saved for future work.

Acknowledgment

This work was supported by Institut de Recherche d'Hydro-Québec and Mathematics of Information Technology and Complex Systems (IT07240). Technologists René Dubois, Alexandre Lapointe, and Manon Provencher are gratefully acknowledged for their help.

References

1. Amrei, M. M., Verreman, Y., Bridier, F., Thibault, D., and Bocher, P. 2015. Microstructure characterization of single and multipass 13Cr4Ni steel welded joints. *Metal., Microstruct., and Anal.* 4(3): 207–218. DOI: 10.1007/s13632-015-0202-8

2. Teske, M., and Martins, F. 2010. The influence of the shielding gas composition on GMA welding of ASTM A 516 steel. *Weld. Int*. 24(3): 222–230. DOI: 10.1080/09507110902843875

3. Foroozmehr, F., Verreman, Y., Chen, J., Thibault, D., and Bocher, P. 2017. Effect of inclusions on fracture behavior of cast and wrought 13% Cr-4% Ni martensitic stainless steels. *Eng. Fract. Mech*. 175: 262–278. DOI: 10.1016/j.engfracmech.2017.02.002

4. Iwabuchi, Y., and Kobayashi, I. 2010. A study of toughness degradation in CA6NM stainless steel. *Mater. Sci. Forum* 654–656: 2515–2518. DOI: 10.4028/www.scientific.net/msf.654-656.2515

5. Wang, P., Lu, S. P., Xiao, N. M., Li, D. Z., and Li, Y. Y. 2010. Effect of delta ferrite on impact properties of low carbon 13Cr-4Ni martensitic stainless steel. *Mater. Sci. and Eng. A* 527(13–14): 3210–3216. DOI: 10.1016/j.msea.2010.01.085

6. Bilmes, P. D., Solari, M., and Lorente, C. L. 2001. Characteristics and effects of austenite resulting from tempering of 13Cr-NiMo martensitic steel weld metals. *Mater. Charact*. 46(4): 285–296. DOI: 10.1016/S1044-5803(00)00099-1

7. Thibault, D., Bocher, P., Thomas, M., Lanteigne, J., Hovington, P., and Robichaud, P. 2001. Reformed austenite transformation during fatigue crack propagation of 13%Cr-4%Ni stainless steel. *Mater. Sci. and Eng. A* 528(21): 6519–6526. DOI: 10.1016/j.msea.2011.04.089

8. Trudel, A., Sabourin, M., Lévesque, M., and Brochu, M. 2014. Fatigue crack growth in the heat affected zone of a hydraulic turbine runner weld. *Int. J. of Fat.* 66: 39–46. DOI: 10.1016/j.ijfatigue.2014.03.006

9. Young, R. A. 1993. *The Rietveld Method*. First Ed. Oxford University Press Inc. USA.

10. ASTM International. 2016. *ASTM E1479. Standard Practice for Describing and Specifying Inductively Coupled Plasma Atomic Emission Spectrometers*.

11. ASTM International. 2011. *ASTM E1019. Standard Test*

Methods for Determination of Carbon, Sulfur, Nitrogen, and Oxygen in Steel, Iron, Nickel, and Cobalt Alloys by Various Combustion and Fusion Techniques.

12. ASTM International. 2017. *ASTM E92. Standard Test Methods for Vickers Hardness and Knoop Hardness of Metallic Materials*.

13. ASTM International. 2016. *ASTM E8. Standard Test Methods for Tension Testing on Metallic Materials*.

14. ASTM International. 2016. *ASTM E23. Standard Test Methods for Notched Bar Impact Testing of Metallic Materials. ASTM International*.

15. ASTM International. 2015. *ASTM A743. Standard Specification for Castings, Iron-Chromium, Iron-Chromium-Nickel, Corrosion Resistant, for General Application*.

16. American Welding Society. 2012. *AWS A5.9, Specification for Bare Stainless Steel Welding Electrodes and Rods*. Eighth Ed. Miami, Fla.

17. Godin, S. Effet d'un enrichissement en nickel sur la stabilité mécanique de l'austénite de réversion lorsque soumise à de la fatigue oligocyclique. Master Thesis. 2014. École de Technologie Supérieure, Montréal.

18. Gooch, T. G., Woollin, P., and Haynes, A. G. 1999. *S99-22, Welding metallurgy of low carbon 13% chromium martensitic steels, supermartensitic stainless steel* 99. Belgian Welding Institute: 188–195.

19. Amrei, M. M., Monajati, H., Thibault, D., Verreman, Y., Germain, L., and Bocher, P. 2016. Microstructure characterization and hardness distribution of 13Cr4Ni multipass weld metal. *Mater. Charact*. 111: 128–136. DOI: 10.1016/j.matchar.2015.11.022

20. Thibault, D., Bocher, P., and Thomas, M. 2009. Residual stress and microstructure in welds of 13% Cr–4%Ni martensitic stainless steel. *J. of Mater. Process. Technol*. 209(4): 2195–2202. DOI: 10.1016/j.jmatprotec.2008.05.005

21. Krauss, G. 2015. *Steels: Processing, Structure, and Performance*. Second Ed. ASM International.

22. Godin, S., Hamel-Akré, J., Thibault, D., Serventi, A.-M., and Bocher, P. 2020. *Ni and Mn enrichment effects on reformed austenite: Thermodynamical and low cycle fatigue stability of 13%Cr–4%Ni and 13%Cr–6%Ni stainless steels*. Springer Nature, accepted for publication on February 4, 2020.

BOUCHRA TENNI and MYRIAM BROCHU (myriam.brochu@polymtl.ca) *are with École Polytechnique de Montréal, Montreal, Canada. STÉPHANE GODIN and DENIS THIBAULT are with Institut de Recherche d'Hydro-Québec, Quebec, Canada.*

The majority of the content in this article was published in the master's thesis Étude expérimentale de l'effet du contenu inclusionnaire sur les propriétés mécaniques de résilience et de fatigue-propagation au seuil de soudures en acier 410 NIMO, by Bouchra Tenni, École Polytechnique de Montréal.